Advanced Functional Materials

ADVANCED FUNCTIONAL MATERIALS
www.afm-journal.de

RESEARCH ARTICLE OPEN ACCESS

High Pressure Densification Investigation of Li_3PS_4 and Li_6PS_5Cl Solid Electrolytes using Combine X-Ray Diffraction, X-Ray Absorption Tomography and Ionic Measurement

Oskar Thompson[1] | Ove Korjus[2] | Adrien Fauchier-Magnan[1] | Clément Albin[3] | Sergio F. Mayer[1] | Emmanuelle Suard[2] | Thomas Hansen[2] | Laura Henry[4] | Nicolas Guignot[4] | Vittoria Pischedda[3] | Sylvie Le Floch[3] | Claire Villevieille[1]

[1]Univ. Grenoble Alpes, Univ. Savoie Mont Blanc, CNRS, Grenoble INP, LEPMI, Grenoble, France | [2]Institut Laue Langevin, Grenoble, France | [3]Institut Lumière Matière, UMR5306 Université Lyon 1-CNRS, Université de Lyon, CEDEX, Villeurbanne, France | [4]Synchrotron SOLEIL, L'orme des Merisiers, Saint-Aubin, France

Correspondence: Sylvie Le Floch (sylvie.le-floch@univ-lyon1.fr) | Claire Villevieille (claire.villevieille@grenoble-inp.fr)

Received: 12 January 2026 | **Revised:** 4 March 2026 | **Accepted:** 20 March 2026

Keywords: high pressure | solid electrolyte | solid-state batteries | synchrotron radiation | thiophosphates materials

ABSTRACT

Proper densification of thiophosphate solid electrolytes is crucial for enhancing ionic transport and for preventing dendrite formation and ensuring mechanical stability. However, achieving optimal densification remains challenging due to the absence of techniques capable of monitoring structural and morphological changes in real time. We design a specific airtight high-pressure cell and clamp, enabling the in situ investigation of amorphous (Li_3PS_4) and crystalline (Li_6PS_5Cl) sulfide-based solid electrolytes. Using X-ray computed tomography and diffraction at the Psiché beamline (SOLEIL synchrotron), we studied the samples under uniaxial compression up to 3700 MPa. We correlate the evolution of structure, density, and porosity with ionic conductivity measurements obtained via electrochemical impedance spectroscopy. The results reveal two densification stages: an initial closure of intergranular porosity, followed by structural densification through elimination of intragranular porosity. The porosity in Li_3PS_4 reduces faster than in Li_6PS_5Cl, reflecting its higher softness. Above 500 MPa, ionic conductivity decreases, likely due to lattice contraction and increased Li^+ migration barriers. Upon decompression, both materials exhibit irreversible conductivity enhancement, attributed to plastic densification and increased structural disorder. These findings highlight the critical role of microstructural control and pressing conditions in optimizing the electrochemical performance of sulfide-based solid electrolytes.

1 | Introduction

Solid-state batteries are widely regarded as promising next-generation energy storage systems, primarily due to their potential for enhanced energy density. Achieving this potential, however, requires solid electrolytes that are both stable against lithium metal and fully densified to eliminate porosity, thereby mitigating dendrite formation. Among the various candidates, thiophosphate-based electrolytes offer a distinct advantage: they can be densified at room temperature (RT) [1, 2], eliminating

Oskar Thompson and Ove Korjus contributed equally to this work.

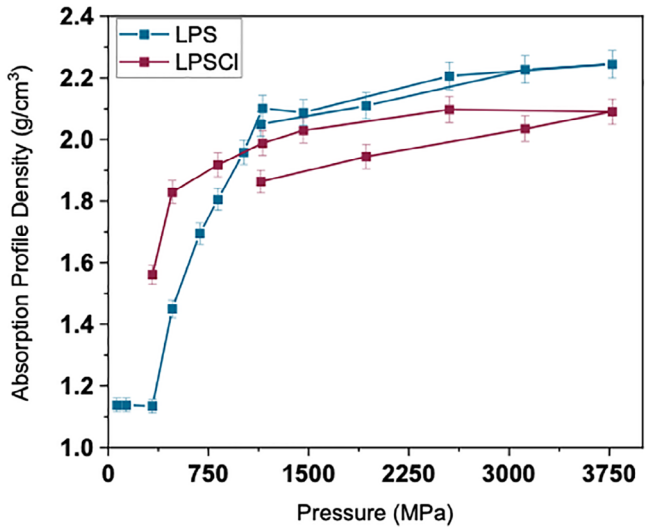

FIGURE 1 | Density, measured with the Beer-Lambert absorption density method, as a function of pressure for both LPSCl and LPS in compression and decompression. Due to a technical issue, measurement at 66 and 135 MPa for LPSCl material are missing.

the need for high-temperature sintering required for oxide electrolytes. Despite this advantage, the morphological and structural evolution of thiophosphate electrolytes during RT densification remains poorly understood, largely due to the absence of in situ characterization techniques capable of monitoring these changes in real time.

Densification is a critical step in solid-state battery fabrication, as ionic conductivity is strongly influenced by porosity [3, 4]. Reduced porosity decreases ionic pathway tortuosity, improves rate capability, and enhances mechanical stability. Conversely, interconnected pores can facilitate lithium dendrite propagation [2, 5, 6], leading to cell failure. Mechanical effects are also inherent to these systems: processing methods such as ball milling can introduce strain into the electrolyte crystal lattice [7], and volume changes during cycling can generate interfacial stress and strain. A comprehensive understanding of the effects of pressure, stress, and strain is thus essential for optimizing electrolyte performance.

Previous studies have explored these effects with unclear outcomes. Ab initio molecular dynamics simulations by Zguns and Yildiz [8] showed enhanced Li-ion diffusivity in β-Li_3PS_4 (LPS) under compressive strain along the c-axis. Yao et al. [9] experimentally applied a reasonably high pressure (~100 MPa) to β-LPS, detecting irreversible structural changes via Rietveld refinement, but without confirming electrochemical benefits. Faka et al. [10] reported contradictory findings for Li_6PS_5Br: in situ impedance spectroscopy showed reduced conductivity above 0.8 GPa, while ex situ measurements up to 10 GPa revealed continuous conductivity gains despite constant activation energy [11]. Nuclear magnetic resonance (NMR) relaxometry suggested longer Li residence times at higher pressures, seemingly inconsistent with electrochemical impedance spectroscopy (EIS) data. These discrepancies were attributed to differences in length scales probed by the techniques and the possible role of dislocations as preferential conduction pathways [12, 13], though experimental confirmation is lacking.

Investigating such complex mechanical–electrochemical interactions in air-sensitive thiophosphate electrolytes under high pressure poses significant experimental challenges. Conventional laboratory methods often limit accessible pressures (<0.5 GPa) and rarely enable simultaneous probing of structural, morphological, and electrochemical properties. Synchrotron-based facilities, such as the Psiché beamline at SOLEIL synchrotron, offer a unique solution by enabling in situ, multi-probe characterization under high pressure, combining X-ray diffraction, X-ray absorption contrast tomography, Beer-Lambert absorption density measurements, and ionic conductivity analysis on the same sample.

In this study, we employ this advanced setup to investigate the densification of Li_6PS_5Cl (LPSCl) and Li_3PS_4 (LPS). Our custom-designed, air-tight sample holder enables compression and decompression without air exposure, allowing direct correlation of structural, morphological, and electrochemical data during densification.

2 | Beer-Lambert Absorption–Density Measurements

We conducted Beer-Lambert absorption density measurements in situ at high pressure using the white beam station of the PSICHÉ beamline following the technique described in Ref. [14]. The density is obtained using the Beer-Lambert absorption law [15] and by scanning the sample along the y-axis at selected energies. In this study, the polychromator and angle of the detector were tuned to 100 keV to obtain an optimal contrast between the sample and the surrounding gasket. When interpreting these data, it is essential to bear in mind that this technique reveals macroscopic density measurement considering all density-related effects, encompassing both morphological (e.g., porosity) and structural (e.g., lattice compression) factors. Figure 1 illustrates the evolution of the absorption profile density of LPS and LPSCl as a function of applied pressure. Due to a technical issue, we could not perform this measurement at 66 and 135 MPa for LPSCl material. For reference, the theoretical densities, obtained at ambient pressure of LPS [16, 17] and LPSCl [18, 19] are 1.85–1.93 $g{\cdot}cm^{-3}$ (based on crystalline LPS) and 1.77–1.88 $g{\cdot}cm^{-3}$, respectively.

Both samples exhibit two distinct stages of densification, characterized by an initial step increase in absorption profile density, followed by a plateau. In the case of LPSCl, the initial rise (up to 500 MPa) can be attributed to the reduction of porosity followed by the beginning of the densification (grains to grains contact, with large particles being broken [20], remaining "nanoporosity" being removed), while the plateau indicates that most of the accessible porosity has been removed and that grains start to deform/break at the lattice scale (in agreement with X-ray diffraction data). For LPS, the tendency is slightly different, with a huge increase in absorption density most probably attributed to the removal of the porosity coupled to the densification of the pellet. Indeed, since LPS is softer than LPSCl, the particles are not breaking and densify instead [2].

In the first stage (below 1 GPa), the density of LPSCl increases rapidly with applied pressure. Notably, at ca. 600 MPa, LPSCl already surpasses its theoretical density and becomes denser than the LPS sample, which only reaches its own theoretical density at ca. 900 MPa. This observation is somewhat counterintuitive, as one might expect the amorphous and mechanically "softer" LPS to densify more readily than crystalline LPSCl. A plausible explanation lies in differences in particle size and morphology between the two materials (See SEM images of both materials in Figure S1). Specifically, densification could be hindered if the LPS powder exhibits greater nanoporous character than LPSCl. This is consistent with their respective synthesis routes: LPS is obtained directly via mechanical synthesis (ball milling) without heat treatment [21], whereas LPSCl synthesis generally involves ball milling followed by a thermal treatment step [22, 23], which can promote particle coarsening and reduce nano-porosity.

The maximum measured density for LPSCl reached 2.10 $g{\cdot}cm^{-3}$, corresponding to ca. 110–120% of its theoretical density (taking the highest and lowest values from the literature). For LPS, the maximum measured density was slightly higher at 2.2 $g{\cdot}cm^{-3}$, equivalent to ca. 113–119% of its theoretical density at ambient pressure (taking the highest and lowest values from the literature for a crystalline LPS). Here, it is worth questioning the accuracy of the theoretical density values reported in the literature. For instance, Sakuda et al. [17] determined the theoretical density of LPS via geometric measurement of a pellet presumed to be fully densified after compaction at 360 MPa and subsequent annealing at 200 °C. However, closer inspection of their X-ray tomography data reveals significant density heterogeneity within the pellet, suggesting that the LPS phase was not completely homogeneous and retained some residual porosity. Given that their publication presents only a single tomography slice, it is difficult to evaluate the extent to which this porosity affects the reported density value.

Upon releasing the pressure from the press, the internal pressure within the sample decreased from ca. 3800 MPa to ca. 1150 MPa (approximately 30% of the maximum applied value). We did not perform the absorption density measurement below this pressure, as we could not guarantee that the sample would still be airtight. A notable difference between the two materials is observed during decompression. For LPS, the density–pressure curve during unloading closely follows that recorded during compression, showing reversibility as would be expected for an amorphous sample with favorable softness. In contrast, LPSCl exhibits slightly lower density values upon decompression, suggesting a greater degree of irreversible (plastic) deformation. Such plastic deformation is generally associated with the formation of dislocations, internal strain, and other crystallographic defect phenomena collectively known as work hardening, which may increase material brittleness [24]. A similar trend was found for the crystallographic density of LPSCl materials, as can be seen in Note S1 and Figure S2. The following section is thus dedicated to the visual observation of the densification of the solid electrolyte by means of the X-ray tomography technique.

3 | In Situ Morphological Evolution

Figure 2 presents a series of reconstructed tomograms of the LPSCl sample densified using the UToPEC press at selected pressures. At an applied pressure of 66 MPa, distinct individual grains are clearly identifiable, as from the absorption density measurement. Both intergranular pores (Figure 2a i. and ii.) and intragranular pores (Figure 2a iii.) are observable within the microstructure. Additionally, a high-density impurity grain (Figure 2 iv.) is visible and has been utilized as a reference marker for image registration, a process that involves the precise alignment and overlay of images from different datasets [25]. Figure 2d depicts the sample after densification at 479 MPa, corresponding to the maximum pressure typically achievable in both the literature and our laboratory-scale cells.

At this pressure, although most intergranular pores have closed, some residual porosity persists. The closure of porosity up to 480 MPa aligns closely with the pronounced increase in absorption profile density observed between 330 and 480 MPa (Figure 1). Moreover, at 480 MPa, intragranular pores remain evident, and the granular microstructure of the electrolyte is still discernible. In contrast, at 1155 MPa, all porosity, including intragranular pores, is eliminated. Given that some pores are located "within" the LPSCl grains, their closure implies either fracturing and subsequent re-densification of the grains or the application of significant stress.

Between 1150 and 1450 MPa, X-ray tomography images do not reveal relevant morphological changes, suggesting that any ongoing transformations occur below the resolution limit of this technique. Notably, the linear region observed in the absorption density profile (Figure 1) starts only at 1450 MPa, indicating the potential persistence of micro- or nanoporous features, smaller than the resolution of the tomography employed. Increasing the densification pressure further to 3800 MPa does not produce additional detectable changes in tomography, corroborating the absorption density measurements.

A comparable investigation was conducted on the amorphous LPS materials, with the corresponding X-ray absorption tomography images presented in Figure 3. At 70 MPa, large individual grains are clearly distinguishable, with the largest grains exhibiting diameters approximately twice those of the largest grains observed in the LPSCl sample. Most of the porosity is localized along the perimeters of these grains (Figure 3a i and ii), while intragranular pores are notably absent. Unlike LPSCl, the synthesis of amorphous LPS does not include a heat treatment step. A high-density impurity, most probably coming from a glovebox pollution, also observed in LPSCl, is present in LPS (Figure 3a iii) and was again used to facilitate image registration. Another noteworthy difference between the tomography datasets of LPS and LPSCl is that the fully densified LPS images appear significantly lighter than their LPSCl counterparts. This difference can be attributed to the higher absolute density of LPS, as confirmed by the absorption profile density measurements (Figure 1).

To examine the microstructural state of the pellets *postmortem*, we recovered the samples that had been densified up to 3700 MPa. Fractographic analysis of these samples provides valuable insights into the material's microstructure and the mechanisms governing crack initiation and propagation.

In Figure 4a, two distinct regions of the solid electrolyte LPSCl are visible: the upper surface, which was in contact with the brass

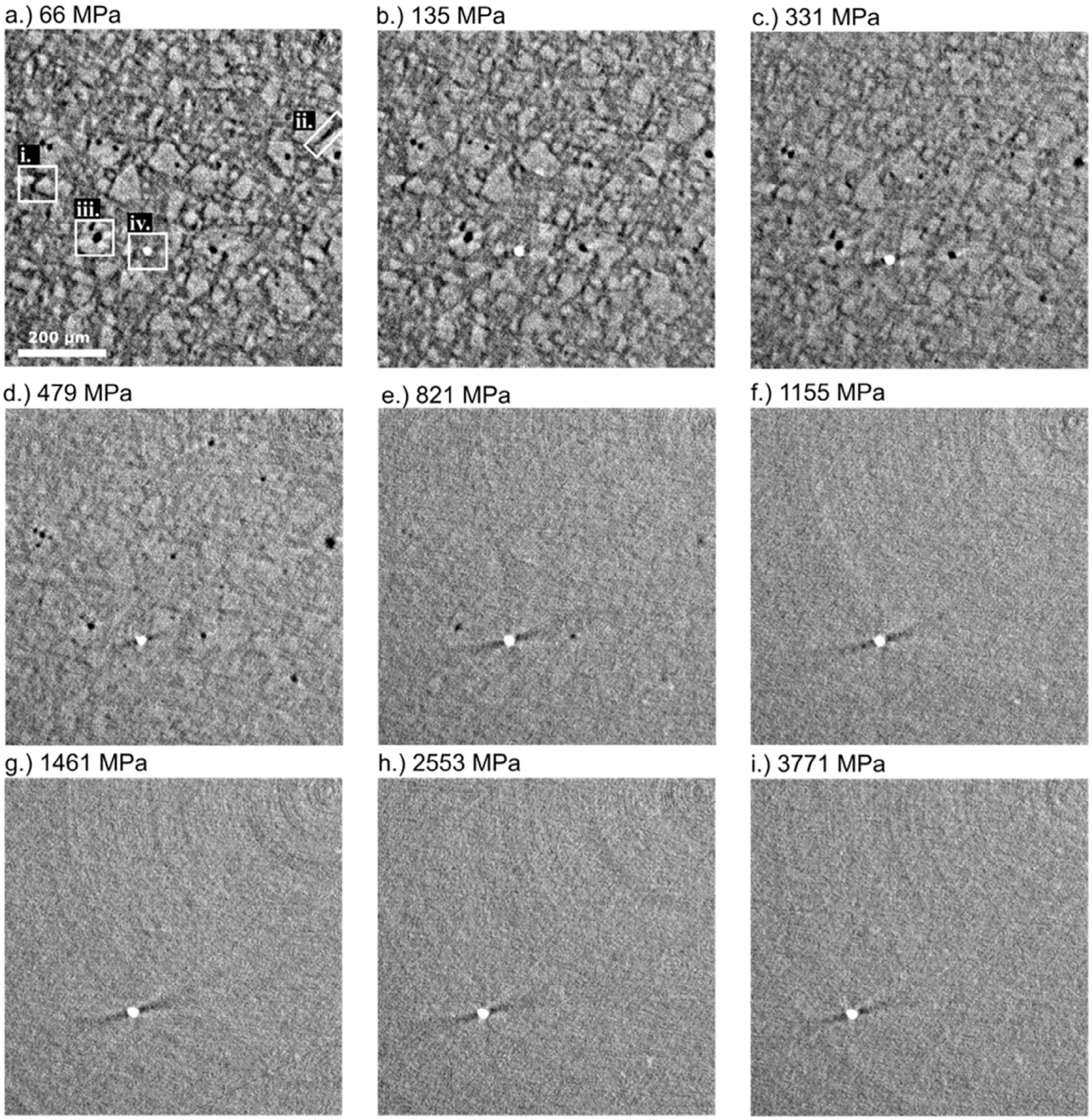

FIGURE 2 | Reconstructed X-ray tomography images of LPSCl during the densification process with three features highlighted: i. & ii.) intergranular pores iii.) intra-granular pores and iv.) impurities. The removal of pores and the merging of grains can be followed as a function of pressure. Voxel size = 1.277 µm.

pin, and the fracture surface of the sample. Figure 4b presents a magnified view of the latter, revealing an inhomogeneous morphology indicative of predominantly intergranular fracture. This fracture mode typically occurs when grain boundary strength is inferior to the bulk strength of the grains [26]. Weak grain boundaries can result from several factors, including crystallographic orientation mismatch and residual intergranular strain. Notably, the pellet exhibited spontaneous fracture several minutes after removal from the Paris–Edinburgh (PE) press. This provides strong evidence of residual stress and strain trapped within the LPSCl sample. These observations are in agreement with the absorption profile density that evolves during decompression, indicating that the densification at room temperature is still not optimal.

The LPS sample (Figure 4c,d) exhibits a comparatively smooth fracture surface. The smaller particles observed on the surface are likely detached fragments adhering electrostatically. On the otherwise flat fracture plane, distinctive striations are visible—referred to as hackle [27]—which are characteristic of rapid brittle fracture occurring once the critical crack propagation velocity has been reached [28].

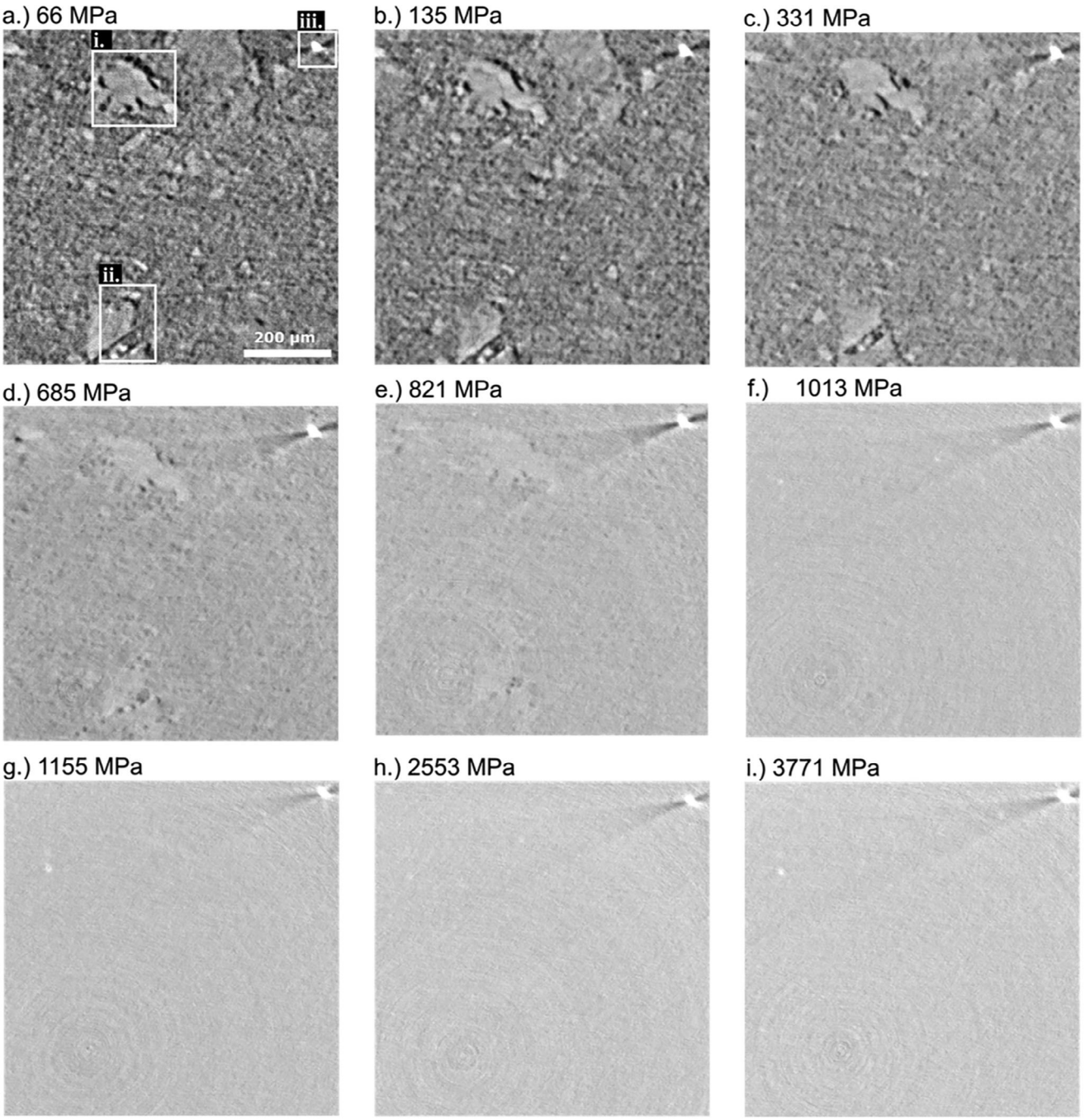

FIGURE 3 | Reconstructed X-ray tomography images of LPS during the densification process with three features highlighted: i. & ii.) inter-granular pores and iii.) impurities. The removal of pores and the merging of grains can be followed as a function of pressure. Voxel size = 1.277 µm.

Although amorphous LPS lacks crystallographic grain boundaries, interparticle contacts remain crucial for achieving high ionic conductivity in the densified electrolyte. The smooth fracture morphology observed here suggests that intimate and homogeneous interparticle contact has been established, as seen in Figure 1 in the absorption density profile, since during the decompression, the LPS value does not change. This contrasts with microstructures obtained via high-temperature sintering, where solid-state diffusion can relieve strain at grain boundaries. In room-temperature densification, by contrast, the absence of such diffusion means that grain boundaries formed under compression remain highly strained. Consequently, even a pellet that appears well densified may be prone to intergranular cracking during electrochemical cycling, leading to reduced ionic conductivity and rate capability.

Amorphous LPS appears less susceptible to this issue due to its lack of long-range crystalline order, which facilitates particle adhesion and the formation of stable agglomerates. This distinction was also noted by Cronau et al. [4], who reported that crystalline LPSCl grains may undergo decohesion in the absence of sufficient stack pressure (200 – 250 MPa), whereas amorphous pellets can maintain structural integrity even at lower pressures.

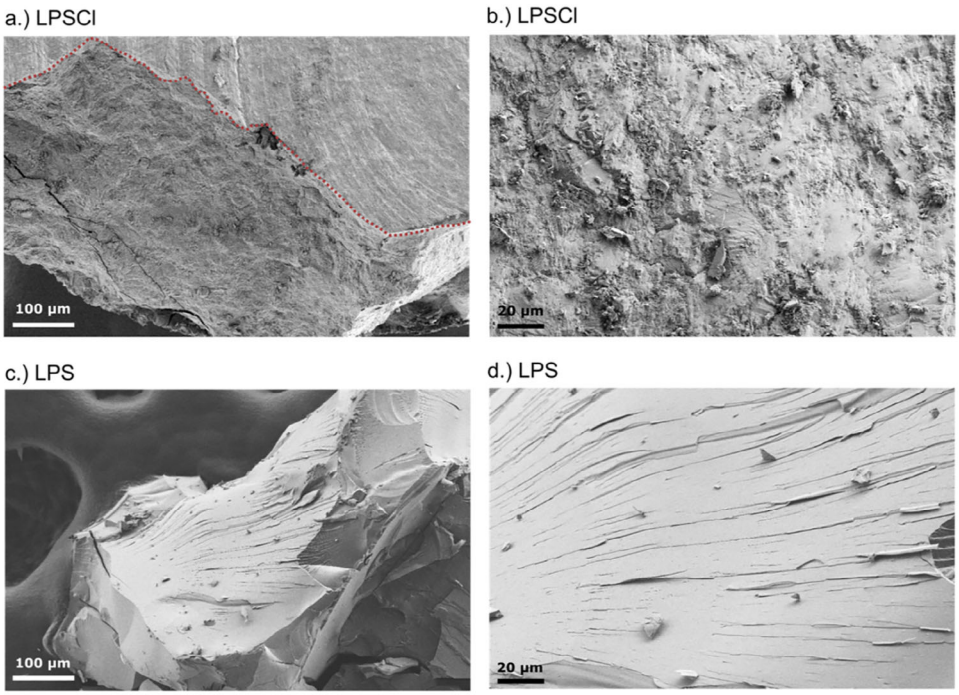

FIGURE 4 | Scanning electron microscopy images taken in secondary electron mode of LPSCl (a,b), and LPS (c,d) showing the fracture surface of the pellets densified at 3.7 GPa. (a) The dotted red line denotes the separation between the upper surface of the pellet that was in contact with the brass pin, and the fracture surface (cross-section).

It is evident that notable morphological changes took place as densification approached 100%. At these elevated pressures, and considering the shrinkage of the pellet, we examined the material's structure to identify any potential distortion or microstrain that may adversely affect ionic conductivity.

4 | In Situ Structural Evolution

4.1 | Energy Dispersive X-Ray Diffraction

To elucidate the structural evolution of LPSCl during densification, we performed in situ high-pressure energy-dispersive X-ray diffraction (ED-XRD). This experiment addressed two primary objectives: (i) to determine whether high-pressure conditions induce the formation of new crystalline phases, and (ii) to assess whether such changes could potentially alter the ionic conduction pathways.

Figure 5 presents a selected region of the Bragg reflections from the LPSCl X-ray diffractograms as a function of applied pressure during both compression and decompression. The complete diffractograms are provided in the Supporting Information (Figure S3). All observed diffraction peaks can be assigned to LPSCl, with no evidence of additional crystalline phases emerging under high pressure.

As expected, increasing pressure results in a shift of the diffraction peaks toward higher scattering angle (this effect is derived from Bragg's Law), consistent with crystal lattice contraction (uniform strain), accompanied by peak broadening (non-uniform strain). A closer look at the diffraction data, especially at pressure around 331 MPa, shows an inversion of the peak intensity for reflections at 30° and 31.5°, without a clear explanation, and could be coming from energy-dispersive X-ray diffraction integration and a faulty detector.

Upon decompression, the peak shift is reversible, in line with elastic lattice strain, whereas the broadening appears largely irreversible, suggesting the development of permanent microstructural defects or disorder.

The observed peak broadening can be ascribed to several microstructural factors, including dislocations, residual microstrains, particle size reduction, and chemical heterogeneities [29]. In general, any phenomenon that disrupts the periodicity of the crystal lattice may contribute to this effect. These microstructural changes can have diverse and sometimes opposing impacts on the electromechanical performance of the solid electrolyte.

For instance, a reduction in crystallite size increases the density of grain boundaries. This is typically detrimental, as grain boundaries can hinder Li-ion transport and promote electrolyte degradation [30, 31]. Similarly, amorphization, characterized by the loss of long-range order, can alter the ionic conduction pathways, potentially reducing ionic conductivity. Conversely, an increased concentration of crystallographic defects may enhance ionic transport. Previous studies have shown that greater site disorder in solid electrolytes can lower the activation energy for Li^+ interstitial hopping, thereby improving conductivity [32, 33].

Since LPS is an amorphous material, no crystalline phase formation was detected during compression or decompression (see Figure S4). Nonetheless, a noticeable shift of the amorphous halo toward higher scattering angles was observed, suggesting the presence of lattice stress that appears to be partially relieved upon

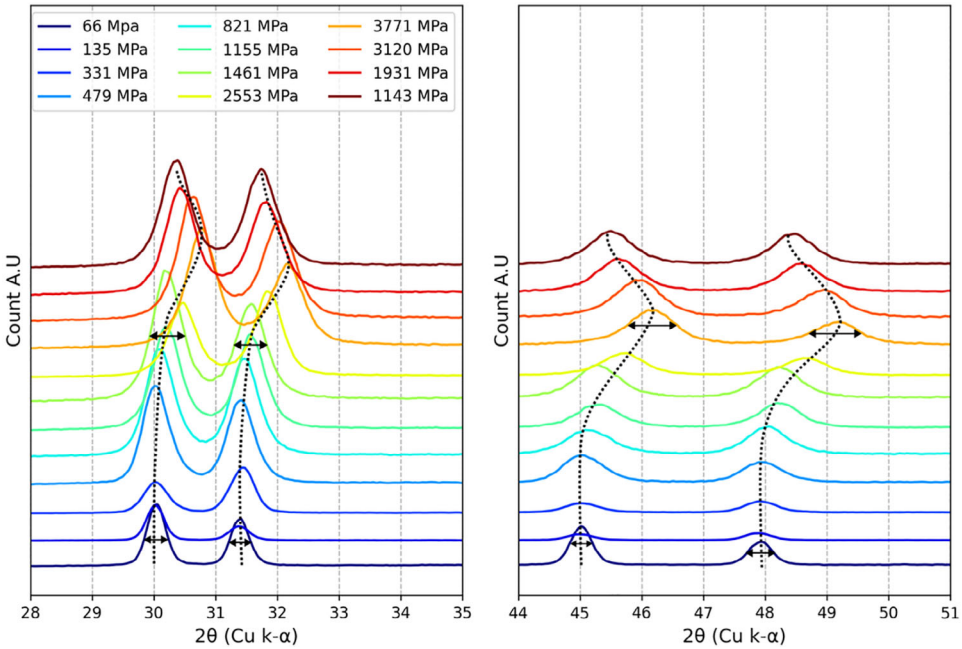

FIGURE 5 | X-ray diffraction data of LPSCl as a function of pressure applied, showing clearly the shifting in peak position and the peak broadening.

pressure release. A quantitative analysis of both isotropic strain—primarily responsible for peak position shifts—and anisotropic strain—associated with peak broadening— is provided in Note S2 and Figures S5 and S6 to gain deeper insight into the structural evolution occurring during densification. We performed neutron powder diffraction (NPD) measurements to complement the study by elucidating Li^+ site position changes occurring under high-pressure conditions.

4.2 | Neutron Powder Diffraction

The NPD anvil cell was slightly different from the cell used for the synchrotron experiment, and lead was added to measure the pressure during compression/decompression processes. Neutron diffraction patterns contain the expected Li_6PS_5Cl and Pb cubic phases, which are displayed in Figure S7, and the pristine sample in the cell is shown in Figure 6a. As shown in Figure S7, three 2θ−regions (43–44.5; 73.4–76, and 89.1–91.4°) were excluded from the refinement, since they contain peaks originating from the cell setup. The widths of the excluded region were slightly adjusted at different pressure points to prevent overlap between peaks from the sample and those from the cell setup.

With increasing applied pressure, the a lattice parameter contracts (Figure 6b), resulting in shorter distances between the ions in the lattice.

At approximately 2609 MPa, Li^+ ions shift 4.9 ± 2.2 % along the x direction in 48h (x,x,z) sites (Figure 7), indicating their relocation in new local energy minima, while the z-coordinate remains unchanged within the limits of detection. This modification on Li coordination is not without consequence on the transport properties of Li ions, a point that will be further discussed in the section dedicated to the ionic conductivity measurement. Upon pressure release and subsequent lattice re-expansion, the Li^+ ions return to their previous position. Additional refined parameters of LPSCl are summarized in Tables S1 and S2.

The maximum lattice strain, indicating the distribution of d-spacings in LPSCl, is presented in Figure 6c as a percentage for each applied pressure. Increased pressure leads to greater anisotropy in lattice spacings, with these changes fully reversible after unloading. Unlike the linear decrease of the lattice parameter with pressure, strain rises exponentially before plateauing above roughly 1000 MPa, reaching 1.75% at 3810 MPa. These results align well with those reported by Faka et al. [10] for Li_6PS_5Br.

Significant morphological and structural modifications occurred during densification of both solid electrolytes. These changes may greatly affect ionic conductivity and transport. To address this, we attempted to measure the samples' ionic conductivity in situ within the high-pressure cell. However, although the experimental setup functioned properly, direct measurements were limited by instrumental constraints. Therefore, we later performed electrochemical impedance spectroscopy (EIS) under similar pressure conditions in the laboratory, where the potentiostat could be connected directly to the anvils, avoiding the restrictions of the synchrotron setup.

5 | Ionic Conductivity Measurements

Figure 8 illustrates the evolution of ionic conductivity as a function of applied pressure for both LPS and LPSCl. In both cases, an initial increase in ionic conductivity is observed during the early stages of densification, coinciding with the reduction of porosity. The maximum ionic conductivity recorded for LPSCl is 3.3 $mS{\cdot}cm^{-1}$ at 135 MPa, while for LPS it is 0.33 $mS{\cdot}cm^{-1}$ at 479 MPa. Beyond these respective maxima, the ionic conductivity of both electrolytes decreases markedly with further pressure

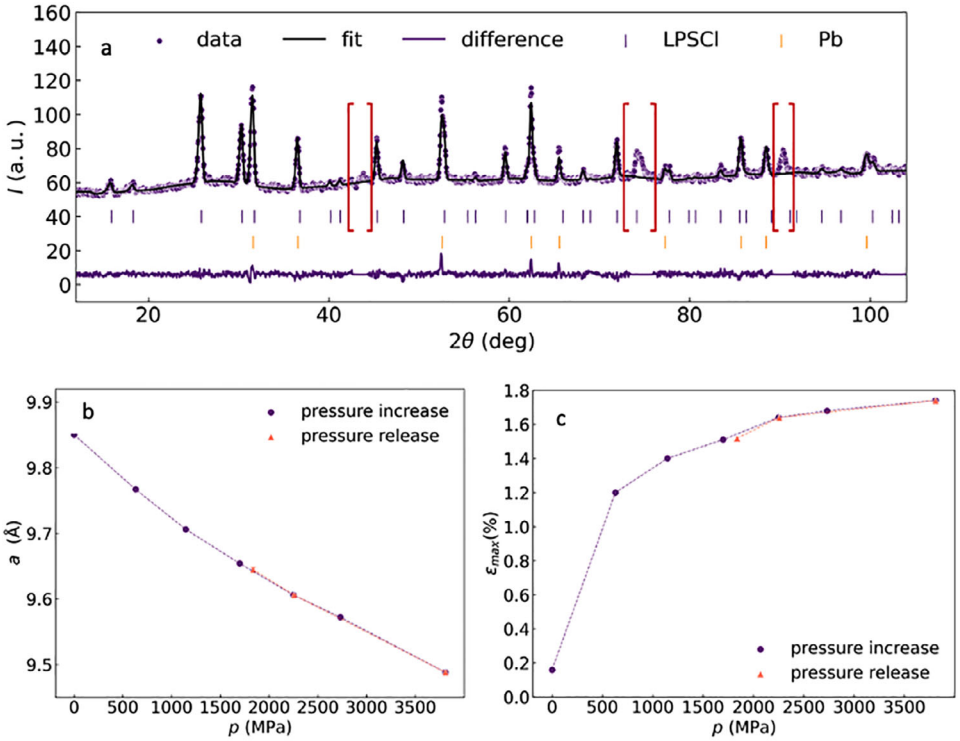

FIGURE 6 | (a) Experimental data (purple points), calculated profiles (black line), and difference curves (purple line) from the Rietveld refinements collected at 0 MPa. Three 2-theta intervals (43–44.5°, 73.4–76°, and 89.1–91.4°), marked with red brackets, were excluded because they contain peaks from the cell assembly. (b) Dependence of lattice parameter and (c) strain on pressure. Purple circles represent pressure increase, and orange triangles represent pressure release.

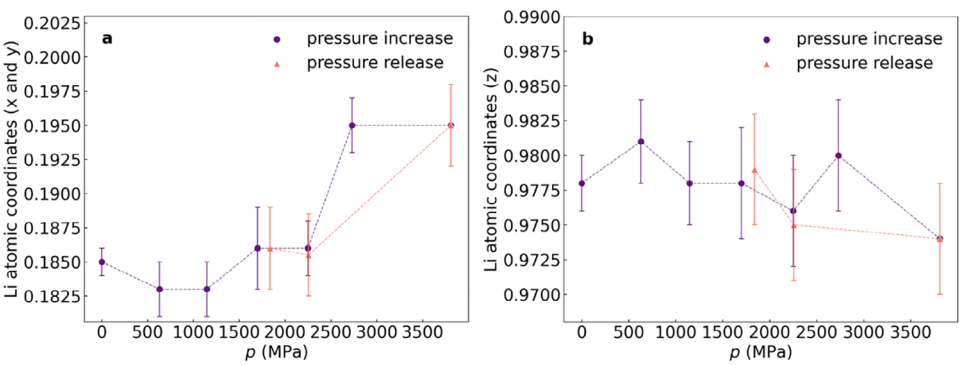

FIGURE 7 | Li atomic position coordinates and their uncertainties at each measured pressure. (a) Fractional coordinates along the x and y directions; (b) fractional coordinate along the z direction.

increase. At the highest applied pressure of 3771 MPa, the conductivities drop to 0.14 mS·cm^{-1} for LPSCl and 0.06 mS·cm^{-1} for LPS.

This phenomenon is likely attributable to the structural evolution of the Li position as a function of the applied pressure. To investigate possible diffusion pathways that could explain the pressure-dependent changes in the ionic conductivity of LPSCl, we calculated bond valence energy landscapes (BVELs) for lithium using the method developed by Adams [34], implemented through the Bond_STR module embedded in the FullProf Suite. Figure 9 displays the LPSCl crystal structure overlaid with the Li^+ BVEL.

The observed decrease in Li-ion conductivity can be attributed to two primary factors. First, the Li-site energy decreases with pressure (Figure 10a), as the shortened interionic distances enhance electrostatic stabilization of the Li sites. Second, the Li-ion percolation activation energy increases progressively with applied pressure (Figure 10b), leading to reduced ionic conductivity. Figure 10b also shows the Li-ion BVELs at three representative pressures (0, 1590, and 3890 MPa) at a constant percolation activation energy cutoff of 0.64 eV. It should be noted that the neglect of relaxation effects in the structure by the BVEL analysis

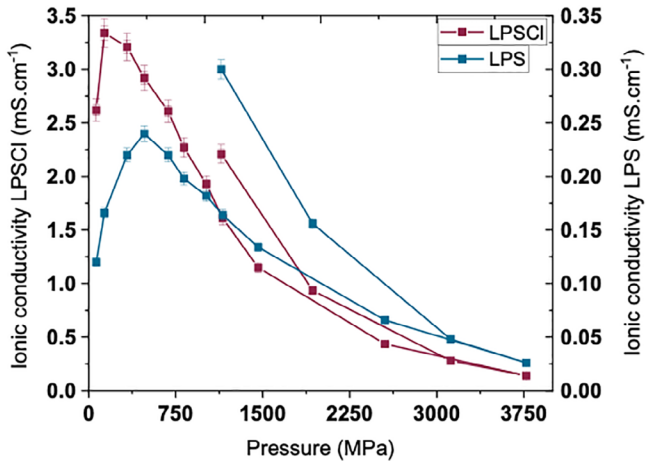

FIGURE 8 | Evolution of ionic conductivity as a function of pressure. The ionic conductivity of LPS is approximately an order of magnitude lower than that of LPSCl; it is therefore plotted with a second y-axis scale on the right-hand side.

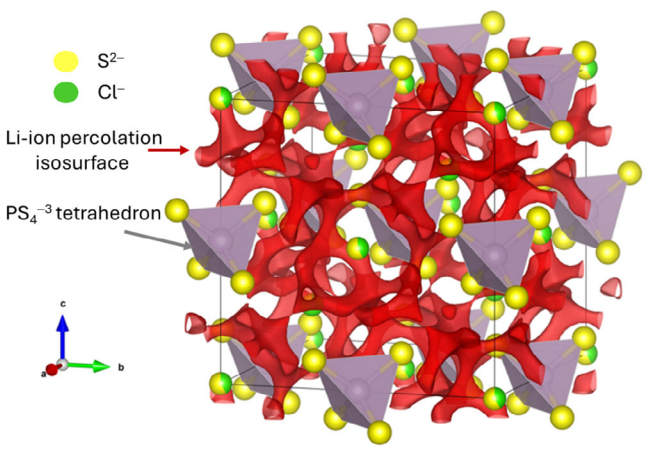

FIGURE 9 | Structure of Li_6PS_5Cl and Li^+ bond-valence energy landscape (BVEL) at 0.64 eV above the site minimum energy at 0 MPa. Red regions indicate Li^+ migration pathways.

leads to an overestimation of the activation energy if compared to other calculation methods, such as density-functional theory [35]. As pressure increases, the connectivity between Li-ion percolation isosurfaces deteriorates. The slight enhancement in ionic conductivity observed between 0 and 135 MPa is most likely associated with improved contact between particles rather than intrinsic changes in the LPSCl crystal lattice.

The following section will quantify the lattice dilation associated with Li^+ site hopping in terms of the activation volume.

6 | Activation Volume

Activation volume is the change in volume when the conducting ion moves from the ground state to the transition state (a.k.a. saddle point). Otherwise stated, activation volume (ΔVa) is the difference between the volume of the lattice at equilibrium (free volume, *Vf*) and its volume required for ion migration (*Vm*). The equations used to calculate the activation volume are reported in Note S3.

Using this method, we determined the activation volume of LPSCl and LPS to be 2.32 and 2.17 $cm^3 \cdot mol^{-1}$, respectively (Figure 11). Because activation volume is not an especially common metric and values for LPSCl have not yet been well established in the literature, it is useful to look at activation volumes that have been declared for other ionic conductors to understand whether the values we have calculated here are reasonable. Famprikis et al. [36] measured the activation volume of Na_3PS_4 up to 700 MPa. They calculated values of 1.78 $cm^3 \cdot mol^{-1}$ for the tetragonal phase and 2.33 $cm^3 \cdot mol^{-1}$ for the cubic phase. Faka et al. [11] calculated activation volumes of between 0.6 and 1.2 $cm^3 \cdot mol^{-1}$ for varying compositions of Li_6PS_5Br. This was extracted from the linear compression region between 0.8 and 1600 MPa. Mellander and Lazarus [37] found that the activation volume of α-Li_2SO_4 is 0.6 $cm^3 \cdot mol^{-1}$ when measuring up to 600 MPa.

7 | Conclusion

Through in situ, multiscale characterization under pressures up to ~4 GPa, this study clarifies how crystalline LPSCl and amorphous LPS solid electrolytes densify and how their structural evolution governs ionic transport. Both materials follow a two-step densification process: rapid porosity collapse followed by lattice-level compaction. Tomography and absorption-density measurements reveal that particle morphology strongly influences the pressure required to eliminate porosity, with LPSCl exhibiting persistent intragranular pores and higher residual strain.

ED-XRD and neutron powder diffraction show that LPSCl retains its crystalline phase but accumulates irreversible defects and lattice strain, whereas amorphous LPS undergoes more homogeneous compression. Ionic conductivity initially increases with improved particle contact but decreases at higher pressures as lattice strain reduces Li-ion pathway connectivity. Overall, moderate pressures aid densification and improve ionic conductivity; upon decompression, both materials exhibit ionic conductivity enhancement compared to compression.

8 | Experimental Section

8.1 | Materials

All sample handling was performed in an argon-filled glovebox to prevent air and moisture exposure. Amorphous Li_3PS_4 solid electrolyte was synthesized via high-energy ball milling. Lithium sulfide (Li_2S, Sigma-Aldrich, 99.98%) and phosphorus pentasulfide (P_2S_5, Sigma–Aldrich, 99%) were weighed to obtain a molar ratio of 75:25 (Li_2S:P_2S_5) and placed in a ZrO_2 milling jar with 5 mm ZrO_2 balls. The mixture was processed in a planetary ball mill (Pulverisette 7, Fritsch) at 510 rpm for 360 cycles, each consisting of 5 min milling followed by 15 min rest. Commercial Li_6PS_5Cl (NEI Corporation) with an estimated particle size of 5 μm was used as received.

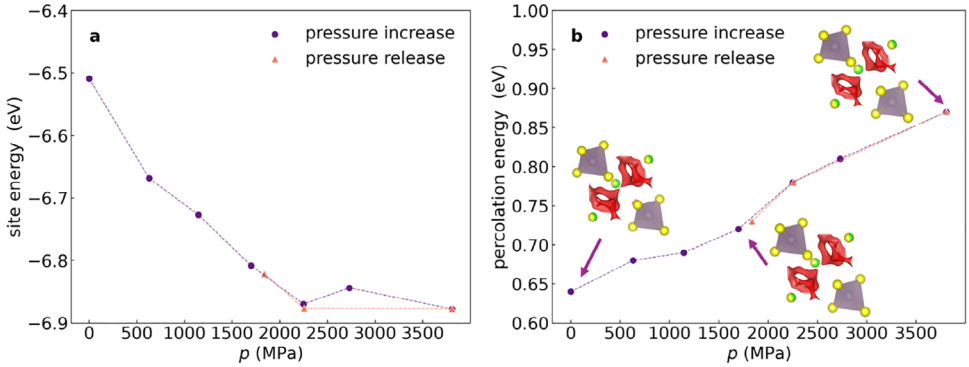

FIGURE 10 | Pressure dependence of (a) percolation energy and (b) Li-site energy, derived from bond-valence calculations. Purple symbols denote increasing pressure, while orange symbols denote pressure release. Bond-valence energy landscapes (BVELs) corresponding to 0 MPa, 1.59 GPa, and 3.89 GPa are shown in panel (b) at a constant percolation activation energy cutoff of 0.64 eV.

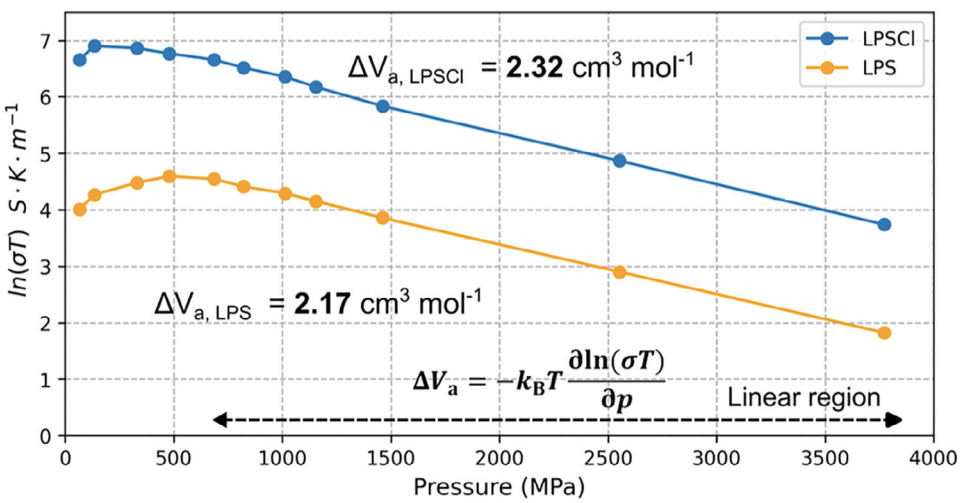

FIGURE 11 | Plot of ln(σT) as a function of pressure. The gradient of this plot can be used to calculate the activation volume of the solid electrolytes.

8.2 | Anvil-Clamp and Paris-Edinburgh Press

The Paris–Edinburgh (PE) press enables the application of pressures up to several tens of gigapascals to solid samples. In this configuration, the use of a pressure-transmitting medium (amorphous boron–epoxy composite) in combination with quasi-conical anvils provides quasi-isostatic compression conditions [38]. In this study, we employed two PE press configurations. The first was a standard PE press, described in detail elsewhere [39]. The second was the Ultra-fast Tomography Paris–Edinburgh Press (UToPEC), a specialized tool available at the Psiché beamline of the SOLEIL synchrotron. The UToPEC press allows sequential in situ measurements of XRD, X-ray absorption tomography, and Beer-Lambert absorption profile, while the sample is progressively compressed or decompressed. This instrument can reach pressures up to 15 GPa [14].

To enable X-ray tomography measurements, the UToPEC press is equipped with a rotation capability, and the lateral pillars are engineered to be exceptionally thin to minimize X-ray attenuation. The anvils and cell components, designed to allow sample assembly entirely within an argon-filled glovebox, are shown in Figure 12b,c. The sample configuration used in the UToPEC press is referred to as "10–3.5," indicating an external gasket diameter of 10 mm and an internal diameter of 3.5 mm.

8.3 | Calibration Curve

In the UToPEC press, the applied load is transmitted via a hydraulic oil pump. The relationship between the applied load and the actual pressure experienced by the sample is established through a calibration curve (Figure S8). Our "10–3.5" setup was calibrated by performing in situ XRD of a NaCl sample loaded in the Teflon tube. The pressure was then estimated using the equation of state of NaCl.

8.4 | Psiché Beamline (X-Ray Computed Tomography and Diffraction)

Energy-dispersive X-ray diffraction (ED-XRD) measurements were performed at the Psiché beamline to probe the structural properties of the solid electrolytes. In this configuration, the broad

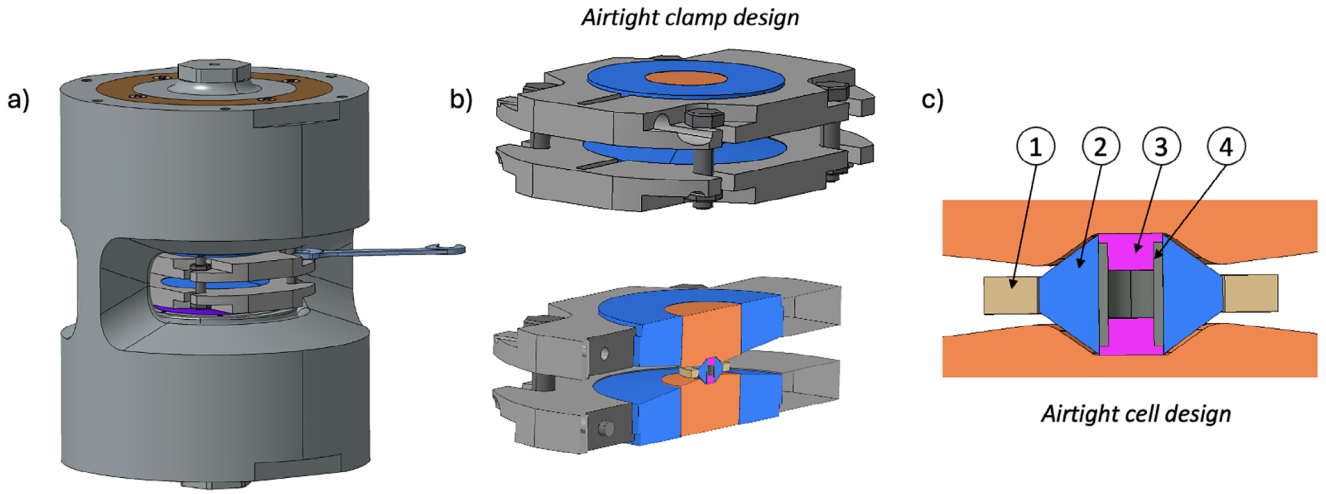

FIGURE 12 | (a) CAD images illustrating the layout of the PE press (UToPEC) at Psiché beamline. (b) Airtight clamp holding the high-pressure cell squeezed between the two anvils, and a cross section of the anvils showing the high-pressure cell, (c) detail of the high-pressure cell with 1-anti-extrusion ring (PEEK); 2-gasket made of amorphous boron-epoxy composite ; 3-brass cap; 4-Teflon (PTFE) tube.

spectrum (white beam 15–100 keV) is diffracted by the sample and recorded simultaneously on seven solid state detectors positioned at fixed scattering angles (~8°) relative to the incident beam. The datasets acquired from the seven detectors are subsequently merged using an in-house Python script developed at the beamline, thereby enabling the reconstruction of a comprehensive diffraction profile.

8.5 | Absorption Density Measurement

X-ray absorption profile is a technique to determine the macroscopic density of a sample, relative to its environment. The measurement is carried out by scanning an X-ray beam horizontally across the diameter of a sample and measuring the X-ray absorption as a function of position (the absorption profile). Knowing the geometry and composition of the sample, it is possible to relate this absorption profile to the sample density using the X-ray form factor, attenuation, and scattering tables of the National Institute of Standards and Technology (NIST) [40]. The sample geometry can be determined by complementary X-ray tomography measurements or can be assumed to be known, depending on the sample. A key advantage of absorption profile density measurements is that they can give reliable density measurements that consider all these potential effects.

8.6 | Electrochemical Impedance Spectroscopy

The impedance measurements were conducted with an SP300 (BioLogic) connected to the anvils of the Paris-Edinburgh press. The spectra were collected at open circuit voltage with a signal amplitude of 10–30 mV (depending on the pressure applied, 30 mV amplitude was used for high-pressure measurement). The impedance was measured in a frequency range from 7 MHz to 10 Hz. Three consecutive EIS spectra were collected upon pressure stabilization. The ionic conductivity values were normalized to the pellet geometry. The Kramers-Kroening linearity test confirmed that the linearity condition was fulfilled in the analyzed frequency region (residuals were under 5%) before the impedance analysis. Analyses were performed with the Relaxis3 software package (RhD instruments, Germany).

8.7 | Neutron Powder Diffraction

About 100 mg of LPSCl was loaded into a spherical TiZr gasket in the glovebox, along with a Pb chip (pressure marker), inside the locking clamp device of the VX Paris-Edinburgh press. Subsequently, the clamp was tightened to exert pressure on the sample (to ensure airtightness), then transferred to the press. It is worth noting that a pressure of 0 MPa corresponds to the pressure in the cell after the clamp is locked, and all the measured pressures in the neutron powder diffraction section are given as a comparison to this value.

D20 beamline, a high-intensity neutron powder diffractometer, was used at the Institut Laue-Langevin (Grenoble, France) for high-pressure diffraction measurements. The wavelength was refined to be 1.539 Å with the $Na_2Ca_3Al_2F_{14}$ standard. The same standard was also used to determine instrumental resolution for microstructure analysis.

Fullprof software was used for Rietveld refinement analysis. Bond valence energy landscapes (BVELs) for lithium were calculated according to a method developed by Adams [34], which has been embedded in the FullProf Suite as the BondSTR embedded module. The software VESTA was used to generate crystal and BVEL images.

8.8 | Data Processing

Reconstructed tomograms were retrieved from the SOLEIL Psiché beamline as h5 files. We then further treated these data using the ImageJ software. Segmentation was performed using Illastik software with a machine learning protocol. The porosity in the electrolyte separator was determined using the

thresholding tool in ImageJ. The threshold is set so that only the darkest grayscale pixels (voids/pores) are selected in the image. The same image processing (brightness, contrast, threshold values, etc.) was used for all images in any given set to ensure a fair comparison.

Acknowledgements

The authors would also like to acknowledge the Agence Nationale de la Recherche Grant OpInsolid for the financial support of this work (ANR-21-CE50-0044). We acknowledged SOLEIL synchrotron for the provision of beamtime under proposal number 20230357 and 20240730.

Open access publication funding provided by COUPERIN CY26.

Conflicts of Interest

The authors declare no conflict of interest.

Data Availability Statement

The data that support the findings of this study are available from the corresponding author upon reasonable request.

References

1. M. Hofer, M. Grube, C. F. Burmeister, P. Michalowski, S. Zellmer, and A. Kwade, "Effective mechanochemical synthesis of sulfide solid electrolyte Li_3PS_4 in a high energy ball mill by process investigation," *Advanced Powder Technology* 34 (2023): 104004.

2. P. Perrenot, A. Fauchier-Magnan, M. Mirolo, et al., "Room-Temperature Sintering of Amorphous Thiophosphate Solid Electrolyte (Li_3PS_4): Coupling Morphological Evolution to Electrochemical Properties," *Advanced Functional Materials* 34 (2024): 2310739.

3. L. Lin, A. Ayyaswamy, Y. Zheng, et al., "Nonintuitive Role of Solid Electrolyte Porosity on Failure," *ACS Energy Letters* 9 (2024): 2387–2393.

4. M. Cronau, M. Szabo, C. König, T. B. Wassermann, and B. Roling, "How to Measure a Reliable Ionic Conductivity? The Stack Pressure Dilemma of Microcrystalline Sulfide-Based Solid Electrolytes," *ACS Energy Letters* 6 (2021): 3072–3077.

5. Z. Ning, G. Li, D. L. R. Melvin, et al., "Dendrite initiation and propagation in lithium metal solid-state batteries," *Nature* 618 (2023): 287–293.

6. J. Kasemchainan, S. Zekoll, D. Spencer Jolly, et al., "Critical stripping current leads to dendrite formation on plating in lithium anode solid electrolyte cells," *Nature Materials* 18 (2019): 1105–1111.

7. O. Maus, M. A. Lange, F. Frankenberg, et al., "Influence of Post-Synthesis Processing on the Structure, Transport, and Performance of the Solid Electrolyte $Li_{5.5}PS_{4.5}Cl_{1.5}$ in All-Solid-State Batteries," *Advanced Energy Materials* 15 (2025): 2403291.

8. P. Žguns and B. Yildiz, "Strain Sensitivity of Li-ion Conductivity in β-Li_3PS_4 Solid Electrolyte," *PRX Energy* 1 (2022): 023003.

9. A. Yao, S. Kadota, S. Hiroi, et al., "In situ structural characterization of Li_3PS_4 solid electrolytes under high pressure," *Journal of Solid State Electrochemistry* 28 (2024): 4401–4407.

10. V. Faka, M. T. Agne, P. Till, et al., "Pressure dependence of ionic conductivity in site disordered lithium superionic argyrodite Li_6 PS_5 Br," *Energy Advances* 2 (2023): 1915–1925.

11. V. Faka, M. T. Agne, M. A. Lange, et al., "Pressure-Induced Dislocations and Their Influence on Ionic Transport in Li + -Conducting Argyrodites," *Journal of the American Chemical Society* 146 (2024): 1710–1721.

12. L. Sun, D. Marrocchelli, and B. Yildiz, "Edge dislocation slows down oxide ion diffusion in doped CeO_2 by segregation of charged defects," *Nature Communications* 6 (2015): 6294.

13. M. Legros, G. Dehm, E. Arzt, and T. J. Balk, "Observation of Giant Diffusivity Along Dislocation Cores," *Science* 319 (2008): 1646–1649.

14. L. Henry, N. Guignot, A. King, E. Giovenco, J.-P. Deslandes, and J.-P. Itie, "In situ characterization of liquids at high pressure combining X-ray tomography, X-ray diffraction and X-ray absorption using the white beam station at PSICHÉ," *Journal of Synchrotron Radiation* 29 (2022): 853–861.

15. https://github.com/EarthianOnEARTH/analysis-package/.

16. L. L. Baranowski, C. M. Heveran, V. L. Ferguson, and C. R. Stoldt, "Multi-Scale Mechanical Behavior of the Li_3PS_4 Solid-Phase Electrolyte," *ACS Applied Materials & Interfaces* 8 (2016): 29573–29579.

17. A. Sakuda, A. Hayashi, and M. Tatsumisago, "Sulfide Solid Electrolyte with Favorable Mechanical Property for All-Solid-State Lithium Battery," *Scientific Reports* 3 (2013): 2261.

18. A. Shao, X. Tang, M. Zhang, M. Bai, and Y. Ma, "Challenges, Strategies, and Prospects of the Anode-Free Lithium Metal Batteries," *Advanced Energy and Sustainability Research* 3 (2022): 2100197.

19. A. Mills, G. Yang, W.-Y. Tsai, et al., "Adverse Effects of Trace Non-polar Binder on Ion Transport in Free-standing Sulfide Solid Electrolyte Separators," *Journal of The Electrochemical Society* 170 (2023): 080513.

20. O. Korjus, S. Mitra, Q. Berrod, et al., "Investigating the densification of Li_6PS_5Cl solid electrolyte through multi-scale characterization techniques," *Energy Storage Materials* 82 (2025): 104589.

21. H. Stöffler, T. Zinkevich, M. Yavuz, et al., "Indris S. Li+-ion dynamics in β-Li_3PS_4 observed by NMR: Local hopping and long-range transport," *The Journal of Physical Chemistry C* 122 (2018): 15954–15965.

22. J. M. Lee, Y. S. Park, J.-W. Moon, and H. Hwang, "Ionic and electronic conductivities of lithium argyrodite Li_6PS_5Cl electrolytes prepared via wet milling and post-annealing," *Frontiers in Chemistry* 9 (2021): 778057.

23. Z. Warren, M. Seghers, P. Boissière, M. Aparicio, and N. C. Rosero-Navarro, "Effect of Temperature during Open Vessel Sintering on Li_6PS_5 Cl Solid-State Electrolyte Powders for Use in Cathode Composite Electrodes," *ACS Electrochemistry* 1 (2025): 1093–1100.

24. J. Pelleg, *Mechanical Properties of Ceramics*, ed. J. Pelleg, (Springer International Publishing, 2014).

25. B. Zitová and J. Flusser, "Image registration methods: A survey," *Image and Vision Computing* 21 (2003): 977–1000.

26. W. Su, L. Chen, S. Huo, W. Zhang, Y. Wang, and Y. Zhou, "Fracture mode transition from intergranular to transgranular in (TiZrNbTaCr)C: The grain boundary purification effect of Cr carbide," *Journal of the European Ceramic Society* 44 (2024): 1881–1889.

27. A. Rabinovitch, G. Belizovsky, and D. Bahat, "Origin of mist and hackle patterns in brittle fracture," *Physical Review B* 61 (2000): 14968–14974.

28. M. He, T. Cheng, Y. Qiao, and H. Li, "A review of rockburst: Experiments, theories, and simulations," *Journal of Rock Mechanics and Geotechnical Engineering* 15 (2023): 1312–1353.

29. T. Ungár, "Microstructural parameters from X-ray diffraction peak broadening," *Scripta Materialia* 51 (2004): 777–781.

30. A. Kushima, S. Koul, Y. Morita, F. Fujisaki, H. Ogasa, and Y. Fujiwara, "In Situ Transmission Electron Microscopy Analysis of Microstructure Evolution of the Li_6PS_5cl Solid Electrolyte in Charge/Discharge Process," *InElectrochemical Society Meeting Abstracts* 240 (2021): 252.

31. E. Milan and M. Pasta, "The role of grain boundaries in solid-state Li-metal batteries," *Materials Futures* 2 (2023): 013501.

32. Y. Xia, J. Li, J. Zhang, et al., "Yttrium stabilized argyrodite solid electrolyte with enhanced ionic conductivity and interfacial stability for all-solid-state batteries," *Journal of Power Sources* 543 (2022): 231846.

33. B. D. Dandena, D.-S. Tsai, S.-H. Wu, W.-N. Su, and B. J. Hwang, "Roles of cation-doped Li-argyrodite electrolytes on the efficiency of all-solid-state-lithium batteries," *Energy Storage Materials* 69 (2024): 103305.

34. S. Adams, "From bond valence maps to energy landscapes for mobile ions in ion-conducting solids," *Solid State Ionics* 177 (2006): 1625–1630.

35. N. A. Katcho, J. Carrete, M. Reynaud, et al., "An investigation of the structural properties of Li and Na fast ion conductors using high-throughput bond-valence calculations and machine learning," *Journal of Applied Crystallography* 52 (2019): 148–157.

36. T. Famprikis, Ö. U. Kudu, J. A. Dawson, et al., "Under Pressure: Mechanochemical Effects on Structure and Ion Conduction in the Sodium-Ion Solid Electrolyte Na_3PS_4," *Journal of the American Chemical Society* 142 (2020): 18422–18436.

37. B. E. Mellander and D. Lazarus, "Electrical conductivity and activation volume for α - Li_2SO_4," *Physical Review B* 31 (1985): 6801–6803.

38. C. L. Bull, A. Bocian, H. Hamidov, K. V. Kamenev, R. J. Nelmes, and J. S. Loveday, "Achieving quasi-hydrostatic conditions in large-volume toroidal anvils for neutron scattering to pressures of up to 18 GPa," *Review of Scientific Instruments* 82, no. 7 (2011): 076101.

39. P. Toulemonde, S. L. Floch, P. Bordet, J. J. Capponi, M. Mezouar, and P. Odier, "In situ study of the synthesis of Hg_2 Ba_2 YCu 2 O 8-δ at high pressure and high temperature by x-ray synchrotron diffraction," *Superconductor Science and Technology* 13 (2000): 1129–1134.

40. C. T. Chantler, K. Olsen, R. A. Dragoset, et al. NIST last modified (2005), http://physics.nist.gov/ffast.

Supporting Information

Additional supporting information can be found online in the Supporting Information section.

Supporting File: adfm75195-sup-0001-SuppMat.docx.